Carbon-Based Electronics: A Computational Study

(Invited Paper)

Mahdi Pourfath and Siegfried Selberherr
Institute for Microelectronics, TU Wien, A-1040 Vienna, Austria
Email: {pourfath|selberherr}@iue.tuwien.ac.at

Abstract— **Carbon-based materials such as carbon nanotubes (CNTs) and Graphene nano-ribbons (GNRs) have been extensively studied in recent years due to their exceptional electronic, opto-electronic, and mechanical properties. We employed the non-equilibrium Green's function (NEGF) formalism to analyze the electronic and optoelectronic properties of CNT- and GNR-based devices numerically. The steady-state and the dynamic response of carbon nanotube-based transistors are studied for a wide range of electron-phonon interaction parameters. The direct band gap and the tuneability of the relatively narrow band gap with the tube diameter or ribbon's width render them as suitable candidates for optoelectronic devices, especially for infrared applications. The performances of CNTs and GNR-based infra-red photo detectors are analyzed.**

I. Introduction

Graphene, a one-atomic carbon sheet with a honeycomb structure, has attracted significant attention due to its unique physical properties [1]. This material shows an extraordinarily high carrier mobility of more than 2×10^5 $\mathrm{cm}^2/\mathrm{V.s}$ [2] and is considered to be a major candidate for future high speed transistor materials. One of the most interesting properties of electrons in graphene is the drastic change of the conductivity with the confinement of the electrons. Structures based on graphene with this behavior are CNTs and GNRs with, respectively, periodic and zero boundary conditions for the transverse electron wave vector. A CNT can be viewed as a rolled-up sheet of graphene with a diameter of a few nanometers. The way the graphene sheet is wrapped is represented by a pair of indices (n, m) called the chiral vector. The integers n and m denote the number of unit vectors along two directions in the honeycomb crystal lattice of graphene. If $m = 0$, the CNT is called *zigzag*. If $n = m$, the CNT is called *armchair*. Otherwise, it is called *chiral*. CNTs with $n-m = 3$ are metals, otherwise they are semiconductors [3]. Semiconducting CNTs can be used as channels for transistors [4], and metallic CNTs can serve as interconnect wires [5]. CNT-based devices have been the subject of intensive research for the last decade [6].

Recently, graphene sheets have been patterned into narrow nanoribbons [7]. These GNRs have attracted much interest as they are recognized as promising building blocks for nanoelectronic devices [8]. The electronic properties of GNRs exhibit a dependence on the ribbon direction and width. In comparison with CNTs, there are some key potential advantages in designing and constructing device architectures based on GNRs [9]. First, all the junctions between GNRs of different width and directionality have a perfect atomic interface, a feature which is difficult to achieve for interfacing CNTs of different diameter and chirality. Second, it is generally difficult to find a robust method to make a contact with a molecular device unit, because there exists usually a large resistance between the metal electrodes and the molecules due to a very small contact area. This difficulty may be circumvented by using GNRs, because the GNR-based devices can be connected to the outside circuits exclusively via semi-metallic GNRs. The direct band gap and the tuneability of the band gap with the tube diameter or ribbons width render CNTs and GNRs as suitable candidates for optoelectronic devices, especially for infra-red applications [10], in particular, due to the relatively narrow band gap [11, 12].

The NEGF method has been successfully utilized to investigate the characteristics of nano-scale silicon transistors [13], CNT-FETs [14–18], and molecular devices [19–21]. In this work we discuss the NEGF formalism to study quantum transport in CNT- and GNR-based devices.

The outline of the paper is as follows. In Section II the NEGF formalism is briefly described. The implementation of this method for CNT- and GNR-based devices is presented in Section III. In Section IV and Section V simulation results are discussed, and conclusions are presented in Section VI.

II. Non-equilibrium Green's Function Formalism

The NEGF formalism initiated by Schwinger, Kadanoff, and Baym allows to study the time evolution of a many-particle quantum system. Knowing the single-particle Green's functions of a given system, one may evaluate single-particle quantities such as carrier density and current. The many-particle information about the system is cast into self-energies which are part of the equations of motion for the Green's functions. A perturbation expansion of the Green's functions is the key to approximate the self-energies. Green's functions enable a powerful technique to evaluate the properties of a many-body system both in thermodynamic equilibrium and non-equilibrium situations.

Four types of Green's functions are defined as the non-equilibrium statistical ensemble averages of the single particle correlation operator [22]. The greater Green's function $G^{>}$ and the lesser Green's function $G^{<}$ deal with the statistics of carriers. The retarded Green's function G^{R} and the advanced Green's function G^{A} describe the dynamics of carriers.

$$
\begin{aligned}
G^{>}(1,2) &= -i\hbar^{-1}\langle\hat{\psi}(1)\hat{\psi}^{\dagger}(2)\rangle \\
G^{<}(1,2) &= +i\hbar^{-1}\langle\hat{\psi}^{\dagger}(2)\hat{\psi}(1)\rangle \\
G^{\mathrm{R}}(1,2) &= \theta(t_1-t_2)[G^{>}(1,2)-G^{<}(1,2)] \\
G^{\mathrm{A}}(1,2) &= \theta(t_2-t_1)[G^{<}(1,2)-G^{>}(1,2)]
\end{aligned} \tag{1}
$$

The abbreviation $1 \equiv (\mathbf{r_1}, t_1)$ is used, $\langle \dots \rangle$ is the statistical average with respect to the density operator, $\theta(t)$ is the unit step function, $\hat{\psi}^{\dagger}(\mathbf{r_1}, t_1)$ and $\hat{\psi}(\mathbf{r_1}, t_1)$ are the field operators creating or destroying a particle at point $(\mathbf{r_1}, t_1)$ in space-time, respectively. The Green's functions are all correlation functions. For example, $G^{>}$ relates the field operator $\hat{\psi}$ of the particle at point $(\mathbf{r_1}, t_1)$ in space-time to the conjugate field operator $\hat{\psi}^{\dagger}$ at another point $(\mathbf{r_2}, t_2)$.

Under steady-state conditions the Green's functions depend only on time differences. One usually Fourier transforms the time difference coordinate, $\tau = t_1 - t_2$, to energy. For example, the lesser Green's function is transformed as $G^{<}(1,2) \equiv G^{<}(\mathbf{r_1}, \mathbf{r_2}; E) = \int (d\tau/\hbar) e^{iE\tau/\hbar} G^{<}(\mathbf{r_1}, \mathbf{r_2}; \tau)$.

Under steady-state conditions the equation of motion for the Green's functions can be written as [23]:

$$
[E-H]\, G^{\mathrm{R,A}}(1,2) - \int d3\; \Sigma^{\mathrm{R,A}}(1,3) G^{\mathrm{r,a}}(3,2) = \delta_{1,2} \tag{2}
$$

$$
G^{\lessgtr}(1,2) = \int d3 \int d4\; G^{\mathrm{R}}(1,3)\Sigma^{\lessgtr}(3,4)G^{\mathrm{A}}(4,2) \tag{3}
$$

H is the single-particle Hamiltonian operator and Σ^{R}, $\Sigma^{<}$ and $\Sigma^{>}$ are the retarded, lesser, and greater self-energies, respectively.

III. Numerical Implementation

This section describes the implementation of the outlined NEGF formalism for the numerical analysis of CNT- and GNR-based devices. A tight-binding Hamiltonian is used to describe the transport phenomena in such devices. The self-energies due to electron-phonon and electron-photon interactions are studied next.

A. Tight-Binding Hamiltonian

In Graphene three σ bonds hybridize in an sp^2 configuration, whereas the other $2p_z$ orbital, which is perpendicular to the graphene layer, forms π covalent bonds. The π energy bands are predominantly determining the solid state properties of graphene. Similar considerations hold for CNTs. We use a nearest-neighbor tight-binding π-bond model [24]. Each atom in an sp^2-coordinated CNT has three nearest neighbors, located $a_{\mathrm{cc}} = 1.42$ Å away. The band structure consists of π-orbitals only, with the hopping parameter $t = V_{pp\pi} \approx -2.7$ eV and zero on-site potential.

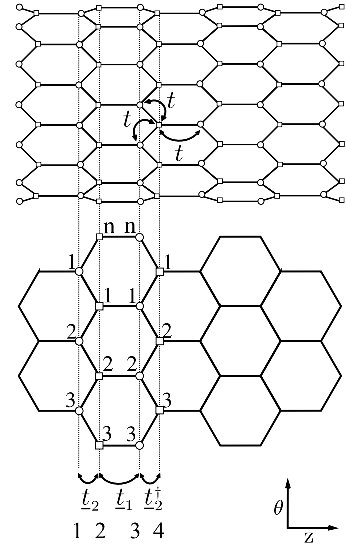

Fig. 1. Layer layout of a $(n, 0)$ zigzag CNT. The coupling matrices between layers are denoted by $\underline{t_1}$ and $\underline{t_2}$, where $\underline{t_1}$ is a diagonal matrix and $\underline{t_2}$ includes off-diagonal elements.

The tight-binding Hamiltonian matrix for a $(n, 0)$ zigzag CNT, shown in Fig. 1, can be written as [24]

$$
\underline{H} = \begin{pmatrix}
\underline{U_1} & \underline{t_2} & & & & \\
\underline{t_2}^{\dagger} & \underline{U_2} & \underline{t_1} & & & \\
 & \underline{t_1} & \underline{U_3} & \underline{t_2}^{\dagger} & & \\
 & & \underline{t_2} & \underline{U_4} & \underline{t_1} & \\
 & & & \underline{t_1} & \underline{U_5} & \cdot \\
 & & & & \cdot & \cdot
\end{pmatrix} \tag{4}
$$

where the underlined quantities denote matrices. We assume that the electrostatic potential shifts the on-site potential. Therefore, $\underline{U_i}$ is a diagonal matrix which represents the electrostatic potential energy in the ith circumferential ring of carbon atoms. Equal electrostatic potential for all carbon atoms within a ring is assumed, therefore $\underline{U_i} = U_i \underline{I}$. The first and second kind of interaction matrix between the neighboring rings are denoted by $\underline{t_1}$ and $\underline{t_2}$. Only the nearest neighbor interaction between carbon atoms is considered. The coupling matrix between Layer 2 and Layer 3 is diagonal, $\underline{t_1} = t\,\underline{I}$, where t is the hopping parameter. However, the coupling matrix between Layer 1 and Layer 2 is given by

$$
\underline{t_2}^{\mathrm{CNT}} = \begin{pmatrix}
t & & & t \\
t & t & & \\
 & t & t & \\
 & & \cdot & \cdot
\end{pmatrix} \tag{5}
$$

Similar matrices can represent the coupling between different layers of armchair GNRs. However, due to different boundary conditions the coupling between Layer 1 and Layer 2 is given by

$$
\underline{t_2}^{\mathrm{GNR}} = \begin{pmatrix}
t & & & \\
t & t & & \\
 & t & t & \\
 & & \cdot & \cdot
\end{pmatrix} \tag{6}
$$

B. Electron-Phonon Self-Energies

A linear dispersion relation for acoustic phonons is assumed, $\omega_{q,\lambda} \approx v_\lambda|q|$, where v_λ is the acoustic phonon velocity and λ is the phonon polarization. For optical phonons the energy is assumed to be independent of the phonon wavevector $\omega_{q,\lambda} \approx \omega_{\mathrm{OP},\lambda} = \mathrm{const}$. Similarly, the matrix elements of electron-phonon interaction [25] can be approximated as $M_{q,\lambda} \approx M_\lambda^{\mathrm{AP}}|q|$ for acoustic phonons and $M_{q,\lambda} \approx M_\lambda^{\mathrm{OP}} = \mathrm{const}$ for optical phonons. The interaction of electrons with optical phonons is inelastic. Assuming that the electron-phonon interaction occurs locally [26] the lesser self-energy can be written as:

$$\Sigma_{\mathrm{inel}}^{<,\nu}(E) = \sum_\lambda D_{\mathrm{inel},\lambda} \times [N_\lambda G^<(E-\hbar\omega_\lambda) \; + \; (N_\lambda+1)\, G^<(E+\hbar\omega_\lambda)] \tag{7}$$

N_λ is the phonon occupation number which is given by the Bose-Einstein distribution function. The electron-phonon interaction strength is given by:

$$D_{\mathrm{inel},\lambda} = \frac{\hbar|M_\lambda^{\mathrm{OP}}|^2}{2nm_{\mathrm{c}}\omega_\lambda} \tag{8}$$

m_{c} is the mass of a carbon atom. The first term in (7) corresponds to the emission of a phonon by the de-excitation of an electron, and the second term corresponds to the excitation of an electron by the absorption of a phonon. The interaction with acoustic phonons can be regarded as elastic scattering, $E \pm \hbar\omega_\lambda \approx E$, and the approximation $N_\lambda \approx N_\lambda + 1 \approx k_{\mathrm{B}}T/\hbar v_\lambda$ can be used. Based on this approximation, the self-energies for acoustic phonon interaction simplify to:

$$\Sigma_{\mathrm{el}}^{\lessgtr,\nu}(E) = D_{\mathrm{el}}^\nu G^{\lessgtr,\nu}(E) \tag{9}$$

$$D_{\mathrm{el},\lambda} = \frac{k_{\mathrm{B}}T|M_\lambda^{\mathrm{AP}}|^2}{nm_{\mathrm{c}}v_\lambda} \tag{10}$$

The self-energy due to electron-phonon interaction comprises the contributions of elastic and inelastic scattering mechanisms, $\Sigma_{\mathrm{e-ph}}^\nu = \Sigma_{\mathrm{el}}^\nu + \Sigma_{\mathrm{inel}}^\nu$.

C. Electron-Photon Self-Energies

The Hamiltonian of the electron-photon interaction can be written as [27, 28]:

$$\hat{H}_{e-ph} = \sum_{l,m} M_{l,m} \left(\hat{b}e^{-i\omega t} + \hat{b}^\dagger e^{+i\omega t}\right) \hat{a}_l^\dagger \hat{a}_m \tag{11}$$

$$M_{l,m} = (z_m - z_l)\,\frac{ie}{\hbar}\sqrt{\frac{\hbar I_\omega}{2N\omega\epsilon c}}\langle l|\hat{H}_0|m\rangle \tag{12}$$

z_m denotes the position of the carbon atom at site m (Fig. 1), I_ω is the flux of photons with the frequency ω, and N is the photon population number. The incident light is assumed to be monochromatic with polarization along the CNT/GNR axis, see Fig. 2. We employed the lowest order self-energy of the electron-photon interaction based on the self-consistent Born approximation [29]:

$$\Sigma_{l,m}^<(E) = \sum_{p,q} M_{l,p}M_{q,m} \times \left[N_\omega G_{p,q}^<(E-\hbar\omega) + (N_\omega+1)G_{p,q}^<(E+\hbar\omega)\right] \tag{13}$$

The first term corresponds to the excitation of an electron by the absorption of a photon, and the second term corresponds to the emission of a photon by de-excitation of an electron.

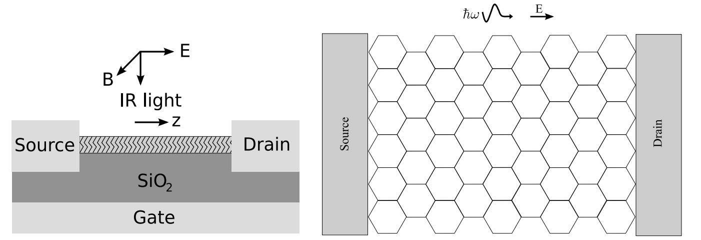

Fig. 2. The sketch of a CNT and GNR-based transistor and photo-detector. The length of the CNT-FET is 50 nm and the length of the photo-detector is 15 nm. In a photo-detector, incident photons generate electron-hole pairs and the electric field drives electrons and holes towards the drain and source contacts, respectively.

IV. CNT-FETs

The electron-phonon coupling strength and the phonon energy depend on the chirality and the diameter of the CNT [25]. In this section the device response is studied for a wide range of electron-phonon interaction parameters. The simulated device structure is shown in Fig. 2.

A. Electron-Phonon Coupling Strength

Fig. 3-a shows the ballisticity as a function of the electron-phonon coupling strength. The ballisticity is defined as $I_{\mathrm{Sc}}/I_{\mathrm{Bl}}$, the ratio of the on-current in the presence of electron-phonon interaction to the current in the ballistic case [30]. The left part of Fig. 3-b illustrates an electron losing its kinetic energy by emitting a phonon. The electron will be scattered either forward or backward. In the case of backward scattering the electron faces a thick barrier near the source contact and

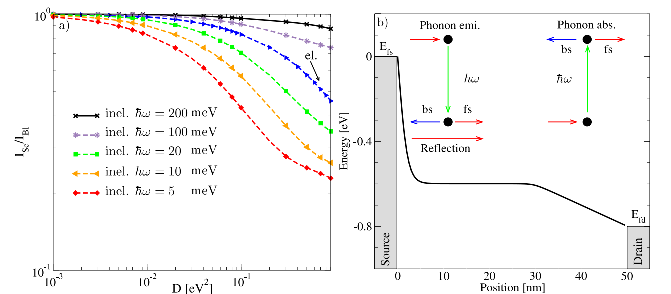

Fig. 3. a) Ballisticity versus electron-phonon coupling strength for a CNT of 50 nm length. Results for both elastic and inelastic scattering with different phonon energies are shown. The operating point is $V_{\mathrm{G}} = V_{\mathrm{D}} = 1$ V. b) Sketch of phonon emission and absorption processes in the channel.

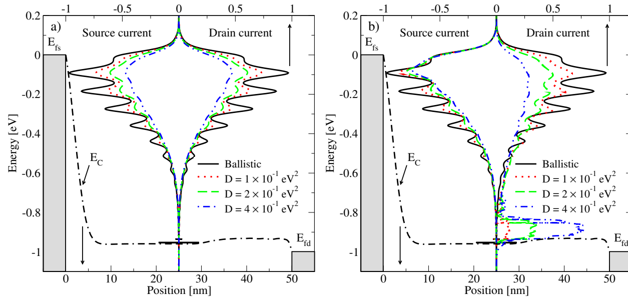

Fig. 4. The spectra of the source and drain currents. a) The effect of elastic phonon scattering with different coupling strengths is shown. b) The effect of inelastic phonon scattering with different coupling strengths is shown. The phonon energy is $\hbar\omega = 100$ meV.

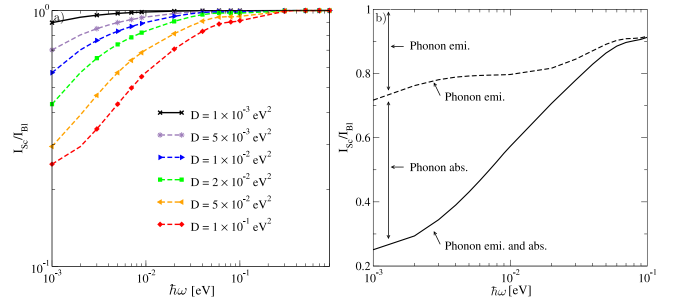

Fig. 5. a) Ballisticity versus phonon energy for a CNT of 50 nm length. Results for inelastic scattering with different electron-phonon couplings are shown. $V_{\rm G} = V_{\rm D} = 1$ V. b) Ballisticity versus phonon energy with $D = 10^{-1}$ eV^2 at the bias point $V_{\rm G} = V_{\rm D} = 1$ V. The contributions due to phonon absorption and emission are shown.

will be reflected with high probability, such that its momentum will again be directed towards the drain contact.

Elastic scattering conserves the energy of carriers, but the current decreases due to elastic back-scattering of carriers. Fig. 4-a shows that for elastic scattering the source and drain current spectra are symmetric. As the electron-phonon coupling strength increases, resonances in the current spectrum are washed out and the total current decreases due to elastic back-scattering. In the case of inelastic scattering, carriers acquiring enough kinetic energy can emit a phonon and scatter into lower energy states. Therefore, as shown in Fig. 4-b, the source and drain current spectra are not symmetric. As the coupling strength increases more electrons are scattered into lower energy states.

B. *Phonon Energy*

Figure 5-a shows the dependence of the ballisticity on the phonon energy. With increasing phonon energy the effect of phonon scattering on the current is reduced, because scattered electrons lose more kinetic energy and the probability for traveling back to the source contact decreases. The considerable decrease of ballisticity for low energy phonons is due to the phonon absorption process. The right part of Fig. 3-b shows an electron absorbing energy from a phonon and scattering into a higher energy state. In this case the probability for arriving at the source contact increases. This process can severely reduce the total current.

Fig. 5-b separately shows the effects of the phonon emission and absorption processes on the ballisticity. As the phonon energy decreases, the phonon occupation number increases exponentially, and the self-energy contributions of these two components increase. However, due to the higher probability for back-scattering of electrons in the case of phonon absorption, this component reduces the total current more effectively than the phonon emission process does.

C. *Switching Response*

To illustrate the effect of electron-phonon interaction on the dynamic response of the device, the gate delay time defined as $\tau = (Q_{\rm on} - Q_{\rm off})/I_{\rm on}$ [31] is considered, where the quasi static approximation is assumed. It has been shown that the quasi static approximation for CNT-based transistors is justified for frequencies below THz [32].

Fig. 6-a shows the ratio of the gate delay time in the ballistic case to that in the presence of electron-phonon interaction, $\tau_{\rm Bl}/\tau_{\rm Sc}$, as a function of the electron-phonon coupling strength. As the phonon energy increases the gate delay time increases. This behavior can be attributed to the average electron velocity in the channel, which is high for ballistic electrons and low for electrons scattered to lower energy states.

Fig. 6-b shows the spectra of the source and drain currents for different inelastic phonon energies. Electrons can emit a single phonon or a couple of phonons to reach lower energy states. The probability of multiple phonon emissions decreases as the number of interactions increases. Therefore, as the phonon energy increases, the occupation of electrons at lower energy states increases. As shown in Fig. 6-b, the electron population close to the conduction band edge considerably increases as the phonon energy increases. Therefore, as the phonon energy increases the mean velocity of electrons decreases and the carrier concentration in the channel increases (Fig. 7). The increased charge in the channel results in an increased gate delay time.

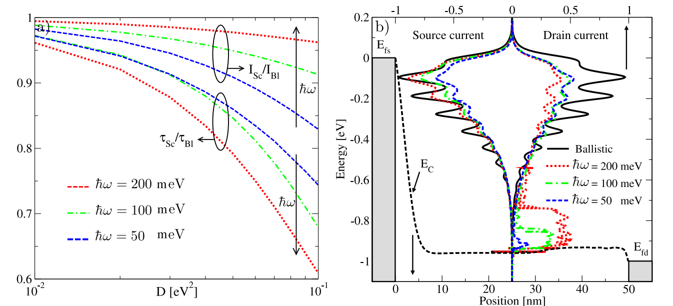

Fig. 6. a) The ratio of the gate delay time in the ballistic case to that in the presence of electron-phonon interaction. For comparison, the ratio $I_{\rm Sc}/I_{\rm Bl}$ is also shown. b) The spectra of the source and drain currents. The effect of inelastic scattering with different phonon energies is shown. The electron-phonon coupling strength is $D = 2 \times 10^{-1}$ eV^2. A considerable increase of the electron population close to the conduction band edge as the phonon energy increases is visible.

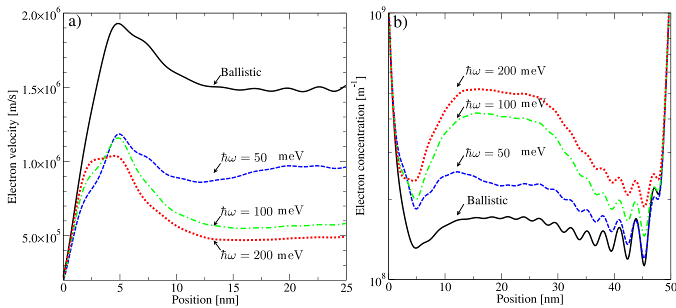

Fig. 7. a) The profile of the electron velocity near the source contact. b) The profile of the electron concentration along the device. The results for the ballistic case and for electron-phonon interaction are shown. As the phonon energy increases the electrons scatter to lower energy states. Therefore, the electron velocity decreases and the carrier concentration increases. The electron-phonon coupling strength is $D = 10^{-1}$ eV^2 and the bias point is $V_{\mathrm{G}} = V_{\mathrm{D}} = 1$ V.

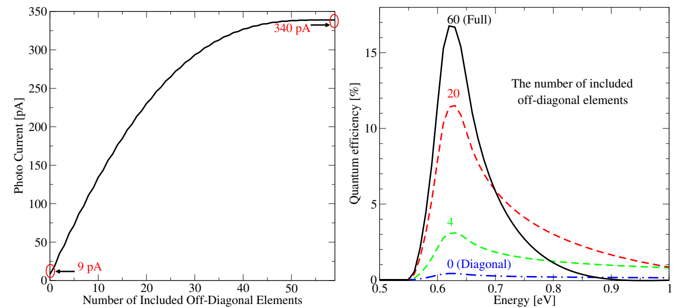

Fig. 8. a) The calculated photo-current as a function of the included off-diagonal elements of the retarded self-energy (Σ^{R}). The full matrix size is 60×60. b) The quantum efficiency of the CNT as a function of the incident photon energy. The number of included off-diagonal elements of the self-energy has a strong influence on the calculated quantum efficiency.

In general the electron-phonon interaction parameters depend on the diameter and the chirality of the CNT [25]. CNTs with a diameter $d_{\mathrm{CNT}} > 2$ nm have a band gap $E_{\mathrm{G}} < 0.4$ eV, which render them unsuitable as channels for transistors. Since the fabrication of devices with a diameter $d_{\mathrm{CNT}} < 1$ nm is very difficult, we limit our study to zigzag CNTs with diameters in the range of $d_{\mathrm{CNT}} = 1-2$ nm. Scattering with acoustic phonons is treated as an elastic process. The electron-phonon coupling is also weak for acoustic phonons ($D_{\mathrm{AP}} < 10^{-3}$ eV^2), which implies that elastic back-scattering of carriers is weak. Inelastic scattering is induced by optical (OP), radial breathing mode (RBM), and K-point phonons [33, 34]. Considering the class of CNTs discussed above, energies of these phonons are $\hbar\omega_{\mathrm{OP}} \approx 200$ meV, $\hbar\omega_{\mathrm{RBM}} \approx 25$ meV, and $\hbar\omega_{\mathrm{K}_1} \approx 160$ meV and $\hbar\omega_{\mathrm{K}_2} \approx 180$ meV [30, 34]. The corresponding coupling coefficients are $D_{\mathrm{OP}} \approx 40 \times 10^{-3}$ eV^2, $D_{\mathrm{RBM}} \approx 10^{-3}$ eV^2, and $D_{\mathrm{K}_1} \approx 10^{-4}$ eV^2, and $D_{\mathrm{K}_2} \approx 10^{-3}$ eV^2 [30]. As discussed in Section IV-B, high energy phonons such as OP and K-point phonons reduce the on-current only weakly, but can increase the gate delay time considerably due to charge pile-up in the channel. Low energy phonons such as the RBM phonon can reduce the on-current more effectively, but have a weaker effect on the gate delay time. However, due to strong coupling, scattering processes are mostly due to electron-phonon interaction with high energy phonons. Therefore, at room temperature the on-current of short CNT-FETs can be close to the ballistic limit [35], whereas the gate delay time can be significantly below that limit [36–38].

The intrinsic (without parasitic capacitances) gate delay time for the ballistic case can be approximated as $\tau \approx 1.7$ ps/μm, or equivalently $f_T \approx 100$ GHz/μm [31]. The highest reported intrinsic cutoff frequency for a device with a length of 300 nm is $f_T \approx 30$ GHz [39], which is far below the ballistic limit. Inelastic electron-phonon interaction with high energy phonon has to be considered to explain the results.

V. PHOTO-DETECTORS

When scattering via a self-energy is introduced, the determination of the Green's function requires inversion of a matrix of huge rank. To reduce the computational cost, the *local scattering approximation* is frequently used [17, 26, 29, 40, 41]. In this approximation the scattering self-energy terms are diagonal in coordinate representation. This allows to employ the recursive algorithm for computing the Green's functions [13, 29]. The local approximation is well justified for electron-phonon scattering induced by deformation potential interaction [41]. However, we show that this approximation is not justified for electron-photon interaction.

For the given CNT device (Fig. 2) the calculated photo current is shown in Fig. 8-a. The current is shown as a function of the number of included off-diagonal elements of the retarded self-energy for electron-photon interaction. By including only the diagonal elements of the self-energy (local scattering approximation) the calculated current is only four percent of its value in case of full matrix consideration. This behavior can be well understood by the fact that the electron-photon self-energy is in general non-local in real space. The off-diagonal elements of the Green's function indicate the correlation between different sites. Due to the wave-like behavior of electrons the correlation length between neighboring sites is on the order of the electron wave length.

To investigate GNR photo-detectors we study the quantum efficiency which is defined as $\alpha = (I_{\mathrm{ph}}/\mathrm{q})/(P_{\mathrm{op}}/\hbar\omega)$, where I_{ph} is the photo current and P_{op} is the incident optical power. Fig. 8-b shows the quantum efficiency of the CNT as a function of the incident photon energy. The efficiency is maximized, when the photon energy matches the band-gap of the CNT. However, at this energy the inclusion of off-diagonal elements becomes more important. This can be understood by the fact that at that peak the carrier energies are close to the conduction and valence band energies, where they have longer wave-lengths. The result is in agreement with experimental data where the maximum quantum efficiency is estimated to be between 10-20 % [11].

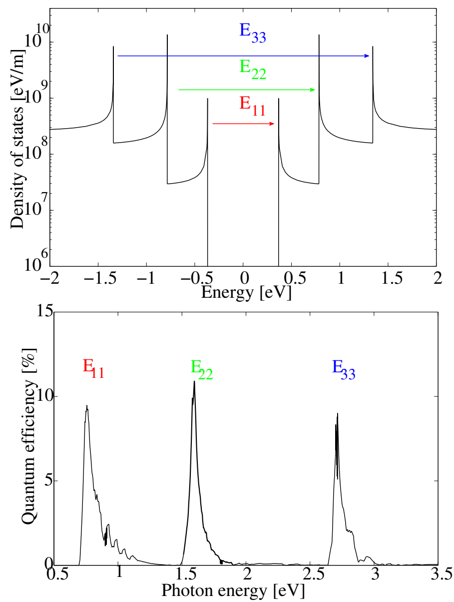

Fig. 9. a) The density of states of an $(12, 0)$ armchair GNR. Some of the most important transitions are marked: E_{ij} denotes a transition from the ith valence band to the jth conduction band. b) The calculated quantum efficiency as a function of the incident photon energy.

Fig. 9-a shows the density for the first three subbands of an $(12, 0)$ armchair GNR. Van Hove singularities in the density of states result in large photon-assisted transitions from the valence to the conduction band [42]. Some of the most important transitions are marked.

Fig. 9-b shows the calculated quantum efficiency of the investigated device as a function of the incident photon energy. The efficiency is maximized, when the photon energy matches the bandgap of the GNR. The maximum quantum efficiency ranges from 9% to 11% and is fairly independent of the bandgap [28]. An experimental and a theoretical study of CNT-based photo-detectors has estimated a quantum efficiency in the $10-20\%$ range [11, 28]. Due to periodic boundary conditions, the subbands of CNTs appear as two-folded degenerate. However, in GNRs this symmetry is removed and subbands are no longer degenerate. It is, therefore, reasonable to expect a maximum quantum efficiency of 10% in GNR devices.

VI. Conclusion

The NEGF method in conjunction with a tight-binding model for the band structure is used to describe transport phenomena in CNT-based devices. Employing the described model, both the static and dynamic response of CNT-FETs was investigated. The effect of electron-phonon interaction on the device characteristics is discussed in detail. In agreement with experimental data, our results indicate that at room temperature electron-phonon interaction affects the steady-state current of CNT-FETs only weakly, whereas the switching response of such devices can be significantly affected. In addition we present a study of CNT- and GNR-based photo-detectors. Due to the lack of band-degeneracy, the photo-current in GNR devices is roughly half of that of their CNT counterparts. Although CNT photo-detectors show better performance, the fabrication of GNRs might be more compatible with current semiconductor technologies, which renders them well suitable for future optoelectronic applications.

Acknowledgment

This work, as part of the European Science Foundation EUROCORES Programme FoNE, was partly supported by funds from FWF (Contract I79-N16).

References

[1] J. Appenzeller, Proc. IEEE **96**, 201 (2008).
[2] X. Du *et al.*, Nature Nanotech. **3**, 491 (2008).
[3] R. Saito *et al.*, Phys. Rev. B **57**, 4145 (1998).
[4] R. Martel *et al.*, Appl. Phys. Lett. **73**, 2447 (1998).
[5] W. Hoenlein *et al.*, IEEE Trans. Comp. Packag. Technol. **27**, 629 (2004).
[6] P. Avouris *et al.*, Nature Nanotechnology **2**, 605 (2007).
[7] C. Berger *et al.*, Science **312**, 1191 (2006).
[8] M. Freitag, Nature Nanotech. **3**, 455 (2008).
[9] Q. Yan *et al.*, Nano Lett. **7**, 1469 (2007).
[10] M. Freitag *et al.*, Phys. Rev. Lett. **93**, 076803 (2004).
[11] M. Freitag *et al.*, Nano Lett. **3**, 1067 (2003).
[12] S. Lu *et al.*, Nanotechnology **17**, 1843 (2006).
[13] A. Svizhenko *et al.*, J. Appl. Phys. **91**, 2343 (2002).
[14] J. Guo, J. Appl. Phys. **98**, 063519 (2005).
[15] J. Guo *et al.*, IEEE Trans. Nanotechnol. **4**, 715 (2005).
[16] A. Svizhenko *et al.*, IEEE Trans. Nanotechnol. **4**, 557 (2005).
[17] A. Svizhenko *et al.*, Phys. Rev. B **72**, 085430 (2005).
[18] M. Pourfath *et al.*, Nanotechnology **18**, 424036 (2007).
[19] W. Tian *et al.*, J. Chem. Phys **109**, 2874 (1998).
[20] Y. Xue *et al.*, Phys. Rev. B **69**, 085403 (2004).
[21] A. W. Ghosh *et al.*, Nano Lett. **4**, 565 (2004).
[22] G. D. Mahan, *Many-Particle Physics*, *Physics of Solids and Liquids*, 2nd ed. (Plenum Press, New York, 1990).
[23] S. Datta, *Electronic Transport in Mesoscopic Systems* (Cambridge University Press, New York, 1995).
[24] J. Guo *et al.*, Intl. J. Multiscale Comput. Eng. **2**, 257 (2004).
[25] V. N. Popov *et al.*, Phys. Rev. B **74**, 075415 (2006).
[26] R. Lake *et al.*, Phys. Rev. B **45**, 6670 (1992).
[27] L. E. Henrickson, J. Appl. Phys. **91**, 6273 (2002).
[28] D. A. Stewart *et al.*, Phys. Rev. Lett. **93**, 107401 (2004).
[29] R. Lake *et al.*, J. Appl. Phys. **81**, 7845 (1997).
[30] S. O. Koswatta *et al.*, Appl. Phys. Lett. **89**, 023125 (2006).
[31] Y. Yoon *et al.*, IEEE Trans. Electron Devices **53**, 2467 (2006).
[32] Y. Chen *et al.*, Appl. Phys. Lett. **89**, 203122 (2006).
[33] R. Saito *et al.*, *Physical Properties of Carbon Nanotubes* (Imperial College Press, London, 1998).
[34] J. Park *et al.*, Nano Lett. **4**, 517 (2004).
[35] A. Javey *et al.*, Nano Lett. **4**, 1319 (2004).
[36] D. Singh *et al.*, IEEE Trans. Nanotechnol. **3**, 383 (2004).
[37] D. Frank *et al.*, IEEE Electron Device Lett. **25**, 34 (2004).
[38] X. Huo *et al.*, in *Intl. Electron Device Meet. Tech. Dig.* 691 (2004)
[39] A. L. Louarn *et al.*, Appl. Phys. Lett. **90**, 233108 (2007).
[40] S. Datta, J. Phys.:Condensed Matter **2**, 8023 (1990).
[41] S. O. Koswatta *et al.*, IEEE Trans. Electron Devices **54**, 2339 (2007).
[42] H. Hsu *et al.*, Phys. Rev. B **76**, 045418 (5pp) (2007).